Laser & Photonics Reviews

LASER & PHOTONICS REVIEWS

www.lpr-journal.org

RESEARCH ARTICLE

Anisotropic Second-Harmonic Ince-Gaussian Beam Generation Using $NbOBr_2$ Holograms

Jayanta Deka[1] | Xiaodong Yang[1] | Jie Gao[2]

[1]Department of Mechanical and Aerospace Engineering, Missouri University of Science and Technology, Rolla, MO, USA | [2]Department of Mechanical Engineering, Stony Brook University, Stony Brook, NY, USA

Correspondence: Xiaodong Yang (yangxia@mst.edu) | Jie Gao (jie.gao.5@stonybrook.edu)

Received: 28 January 2026 | **Revised:** 5 May 2026 | **Accepted:** 3 June 2026

Keywords: 2D materials | Ince-Gaussian beam | optical anisotropy | second-harmonic generation

ABSTRACT

Ince-Gaussian (IG) modes are a complete and orthogonal set of solutions to the paraxial wave equation in elliptic coordinates representing a continuous transition between Hermite-Gaussian modes and Laguerre-Gaussian modes. Chip-scale platforms to generate IG beams have great significance for various applications, including optical trapping and micromanipulation of particles, optical communication, and quantum optics. On the other hand, materials with high optical anisotropy are crucial for building polarization-sensitive optical devices. In this context, niobium oxide dihalides are a new class of ferroelectric materials exhibiting strong, tailorable, and highly anisotropic second-harmonic generation responses. Here, we report the generation of highly anisotropic second-harmonic IG beams using binary grating holograms patterned on ultrathin niobium oxide dibromide ($NbOBr_2$) flakes. Both even and odd IG beams with different mode indices are generated by encoding the phase profiles of the beams into the holograms. According to the polarization-dependent second-harmonic generation responses, the relative magnitudes of the second-order nonlinear susceptibility elements of $NbOBr_2$ crystal are extracted. The results presented here provide new directions for generating complex optical beams with potential applications in classical and quantum photonic integrated devices.

1 | Introduction

Hermite-Gaussian (HG), Laguerre-Gaussian (LG), and Ince-Gaussian (IG) modes are complete and orthogonal sets of solutions to the paraxial wave equation in cartesian, cylindrical, and elliptic coordinates, respectively. IG modes possess both radial and elliptical symmetries and can be described by the Ince polynomials together with the ellipticity parameters. Besides, IG modes represent a continuous transition between HG modes and LG modes as the ellipticity parameter varies from zero to infinity. As such, IG beams are considered as a more general class of higher-order Gaussian beams generated inside a laser cavity [1, 2]. IG beams have stable beam structures with their shapes remaining unchanged during propagation, behaving similarly to the fundamental Gaussian beam. The spatial structures of IG beams, their orthogonality, along with the continuous tunability of their profiles through the ellipticity parameter, make them suitable for a variety of applications, including optical trapping and micromanipulation [3], optical communication [4, 5], optical mode conversion [6–8], and quantum optics [9, 10]. The IG beams are orthogonal to each other, allowing the mode indices to be used as additional degrees of freedom for increasing data capacity in optical communication using mode-division multiplexing [11, 12]. The large number of transverse IG modes along with their propagation characteristics similar to the fundamental Gaussian beam, enables the use of IG beams to create a variety of transverse optical potential landscapes for the ordered, optically guided trapping of particles [13]. Besides possessing two mode indices, the IG beams

https://doi.org/10.1002/lpor.71443

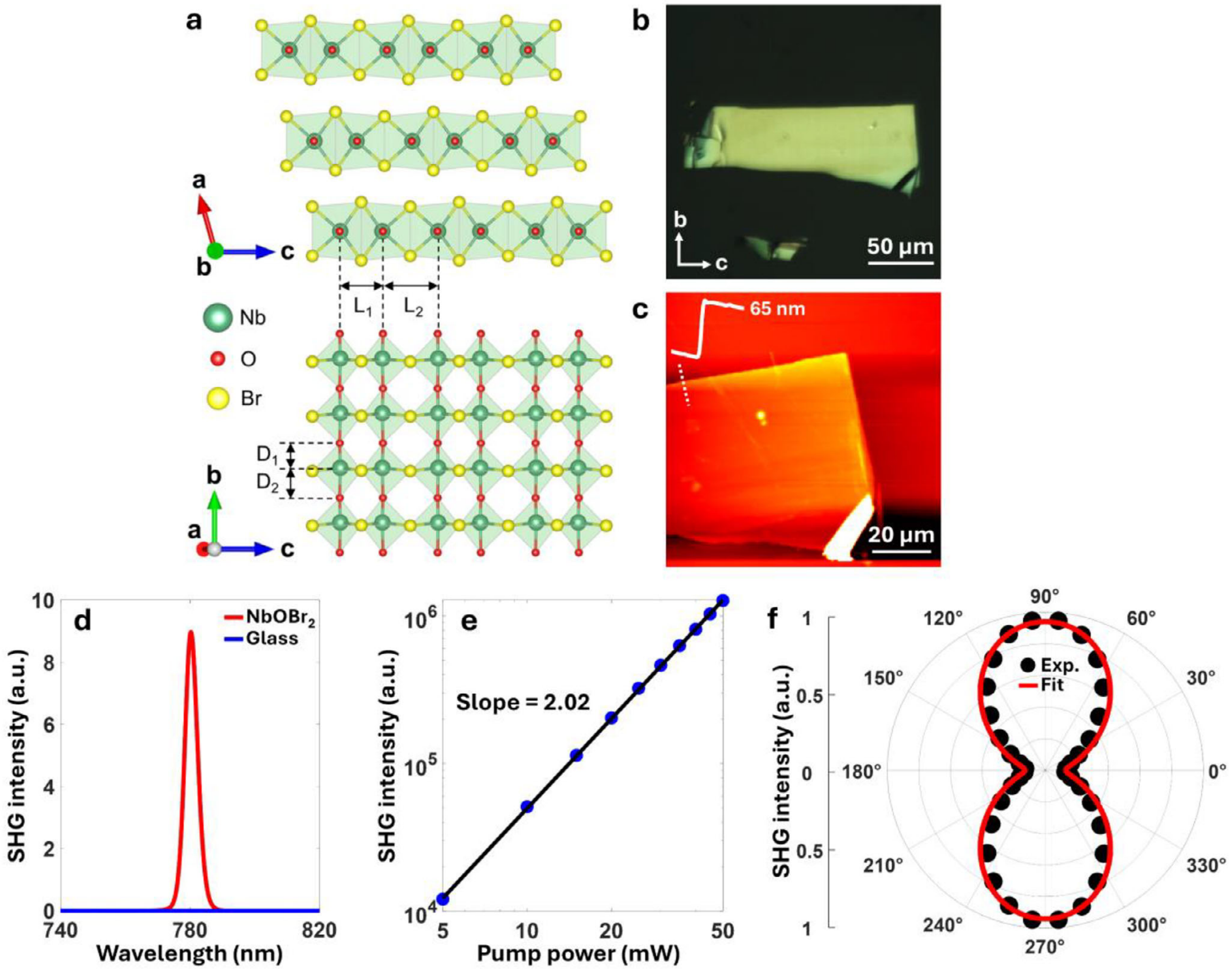

FIGURE 1 | (a) Schematic illustration of the $NbOBr_2$ crystal structure. L_1 and L_2 are the two unequal Nb—Nb distances along the *c*-axis, while D_1 and D_2 are the two unequal Nb—O distances along the *b*-axis induced by Peierls distortion. (b) Optical microscope image of the $NbOBr_2$ flake transferred on a glass substrate. The crystallographic *b* and *c* axes are shown in the inset. (c) AFM image of the flake with the line scan shown in the inset. (d) SHG spectrum measured on the $NbOBr_2$ flake and on the glass substrate at the excitation wavelength of 1560 nm shown as red and blue solid lines, respectively. (e) SHG intensity as a function of the excitation power plotted in a log–log scale. (f) Measured SHG intensity as a function of the excitation linear polarization angle (black dots) and the theoretical fit (red solid line).

have the ellipticity parameter as an additional degree of freedom, making them suitable for producing high-dimensional entanglement and enhanced entanglement for applications in quantum optics [9, 10]. In addition, the IG beam or other complex optical beam generation in the nonlinear regime has advantages over the beam generation in the linear regime for specific applications such as optical communication with nonlinear wave mixing and entangled structured photon sources for quantum information processing [14, 15]. The traditional methods of producing IG beams require spatial light modulators and other bulky optical components [16–18]. Therefore, chip-scale platforms to generate IG beams are of great significance in integrated photonic devices, which have remained largely unexplored in the existing literature. The generation of IG beams in miniaturized platforms has been demonstrated previously using plasmonic metasurfaces [19], and holography-based devices [20–22]. However, plasmonic metasurfaces often suffer from high losses, low damage thresholds, together with low conversion efficiencies. The second-harmonic holography-based devices to generate IG beams on the lithium niobate platform have the limited conversion efficiencies due to the phase-matching constraints [20]. In this context, two-dimensional (2D) materials with strong second-order nonlinear optical responses represent an emerging platform to realize various functional nonlinear optical devices at the nanoscale [23–25]. Meanwhile, the highly anisotropic optical responses of various 2D materials have gained significant research interest for developing next-generation polarization-sensitive photonic devices [26–28]. Particularly, niobium oxide dihalides $NbOX_2$ (X = Cl, Br, I) are a new class of 2D materials with inherent broken inversion symmetry arising from their unique ferroelectric crystal structures exhibiting one-dimensional Peierls distortion. This group of materials has been reported to have strong and highly anisotropic second-harmonic generation (SHG) responses, which vary with wavelength and can be tuned by various external stimuli such as pressure, strain, or temperature [29–36]. The versatile second-order nonlinear optical properties of these crystals have been applied to build various nanoscale advanced photonic devices [30, 32, 36, 37]. Additionally, other materials such as the perovskite microwire arrays and the MoS_2/TiO_2 nanowire hybrid structures have also been introduced to exhibit anisotropic nonlinear optical properties [38, 39].

Here, we demonstrate the generation of highly anisotropic second-harmonic IG beams based on the binary grating holograms imprinted on $NbOBr_2$ flakes. The holograms are patterned on $NbOBr_2$ thin flakes for modulating the second-order nonlinear susceptibility of the crystal to produce the second-harmonic IG beams in the first diffraction order. The $NbOBr_2$ crystal is first characterized with its anisotropic SHG response to identify its crystallographic orientation. Next, both even and odd IG beams with different mode indices are generated by encoding the phase profiles of the beams into the $NbOBr_2$ binary grating holograms. The polarization-dependent SHG measurements reveal that the generated IG beams exhibit highly anisotropic responses due to the unique crystal structure of the $NbOBr_2$ lattice. According to the theoretical fits of the polarization-dependent SHG intensities, the relative magnitudes of the second-order nonlinear susceptibility elements of $NbOBr_2$ crystal are retrieved for both the bare flakes and the fabricated holograms. The results demonstrated here open new avenues for the realization of ultracompact chip-scale platforms to generate polarization-sensitive complex optical beams for potential applications in optical trapping, optical communication, and quantum optics.

2 | Results and Discussion

The $NbOBr_2$ crystal structure is displayed in Figure 1a. The 2D atomic layers of $NbOBr_2$ crystal in the *bc*-plane are stacked together by the weak van der Waals force along the out-of-plane *a*-axis with the individual layer thickness of 7.02 Å [32]. The crystal exhibits a one-dimensional Peierls distortion where Nb atoms are displaced from the center positions, resulting in the unequal distances between two Nb atoms along the *c*-axis (L_1 = 3.14 Å, L_2 = 3.88 Å) and the unequal distances of the Nb atom from two neighboring O atoms along the *b*-axis (D_1 = 1.80 Å, D_2 = 2.11 Å) [40]. This creates strong spontaneous polarization along the *b*-axis or the polar axis resulting in strong second-order optical nonlinearity. The $NbOBr_2$ crystal also exhibits a highly anisotropic SHG response due to low in-plane crystal symmetry, with the much stronger SHG emission when excited along the polar axis (*b*-axis) compared to the excitation along the non-polar axis (*c*-axis). The $NbOBr_2$ crystal is characterized for SHG response along with its polarization dependence, which can be utilized to identify the crystallographic orientation. Figure 1b shows the optical microscope image of one $NbOBr_2$ flake mechanically exfoliated from the bulk crystal on a glass substrate. The atomic force microscopy (AFM) image of the flake is displayed in Figure 1c, together with the line scan of the AFM image showing the thickness of around 65 nm. The SHG spectrum of the flake excited by a 1560 nm pump laser is shown in Figure 1d, showing a peak around 780 nm which is exactly half of the pump wavelength. The excitation power dependence of the generated SHG signal is plotted in a log-log scale in Figure 1e, showing a slope of 2.02, which confirms the SHG process. The polar plot of the SHG intensity as a function of the excitation linear polarization angle is shown in Figure 1f, depicting a highly anisotropic two-lobe pattern. The orientation corresponding to the maximum SHG intensity in the polarization-dependent profile can be identified as the *b*-axis of the $NbOBr_2$ crystal. Since $NbOBr_2$ crystal belongs to the monoclinic structure with the C2 space group, the polarization-dependent SHG intensity can be expressed as [30]

$$I_{2\omega} \propto \left|3\chi^{(2)}_{bcc} cos^2\theta sin\theta + \chi^{(2)}_{bbb} sin^3\theta\right|^2 + \left|\chi^{(2)}_{bcc} cos^3\theta - 2\chi^{(2)}_{bcc} sin^2\theta cos\theta + \chi^{(2)}_{bbb} sin^2\theta cos\theta\right|^2 \quad (1)$$

where θ is the excitation linear polarization angle with respect to the crystallographic *c*-axis, $\chi^{(2)}_{bbb}$ and $\chi^{(2)}_{bcc}$ are the two independent elements of the second-order nonlinear susceptibility of the $NbOBr_2$ crystal. The theoretical fit to the experimental data is also plotted in Figure 1f as the solid line which shows good agreement with the measured data. The crystallographic orientation of the *b* and *c* axes for the $NbOBr_2$ flake is illustrated in the inset of Figure 1b as identified from the polarization-dependent SHG intensities.

In the elliptic coordinates, the transverse spatial profile of the IG beam with order *p*, degree *m*, and ellipticity parameter ε at the plane $z = 0$ can be written as [1, 2]

$$IG^{e}_{p,\,m}(r,\varepsilon) = A\, C^{m}_{p}(i\xi,\varepsilon)\, C^{m}_{p}(\eta,\varepsilon) \exp\left(-\frac{r^2}{w_0^2}\right) \quad (2)$$

$$IG^{o}_{p,\,m}(r,\varepsilon) = B\, S^{m}_{p}(i\xi,\varepsilon)\, S^{m}_{p}(\eta,\varepsilon) \exp\left(-\frac{r^2}{w_0^2}\right) \quad (3)$$

The superscripts *e* and *o* denote the even and odd modes, respectively. *A* and *B* represent the normalization constants. C^m_p and S^m_p are the even and odd Ince polynomials of order *p*, degree *m*, and ellipticity parameter ε, respectively. The parameters *p* and *m* have the same parity, satisfying the relation $(-1)^{p-m} = 1$, and they are related as $0 \le m \le p$ for even Ince polynomials and $1 \le m \le p$ for odd Ince polynomials. ε is the ellipticity parameter defined as $\varepsilon = 2f_0^2/w_0^2$, where f_0 is the semifocal separation and w_0 is the beam width at the plane $z = 0$. *r* is the radial distance in the *z*-plane. (ξ, η) denote the radial and angular elliptic coordinates, with $\xi \in [0, \infty)$ and $\eta \in [0, 2\pi)$. The elliptic coordinates (ξ, η) are related to the Cartesian coordinates (x, y) with $x = f_0 \cosh(\xi)\cos(\eta)$ and $y = f_0 \sinh(\xi)\sin(\eta)$. The transverse spatial profile of the IG beam is determined by the order *p*, degree *m*, and ellipticity parameter ε. Here, the elliptical parameter ε is 2, and different IG beams of $IG^e_{4,\,2}$, $IG^e_{5,3}$ and $IG^o_{4,\,2}$, $IG^o_{5,3}$ are considered. The phase profile $\phi(x, y)$ of the IG beam in cartesian coordinates is used for creating the holograms by assuming the amplitude profile $A(x, y) = 1$.

The binary modulation of the second-order nonlinear susceptibility of the $NbOBr_2$ crystal required to generate the IG beam in the first diffraction order can be expressed as,

$$\chi^{(2)}(x,y) = \chi^{(2)}\left\{\frac{1}{2} + \frac{1}{2} sgn\left[cos\left\{\frac{2\pi x}{\Lambda} - \phi(x,y)\right\} - cos\left\{sin^{-1}A(x,y)\right\}\right]\right\} \quad (4)$$

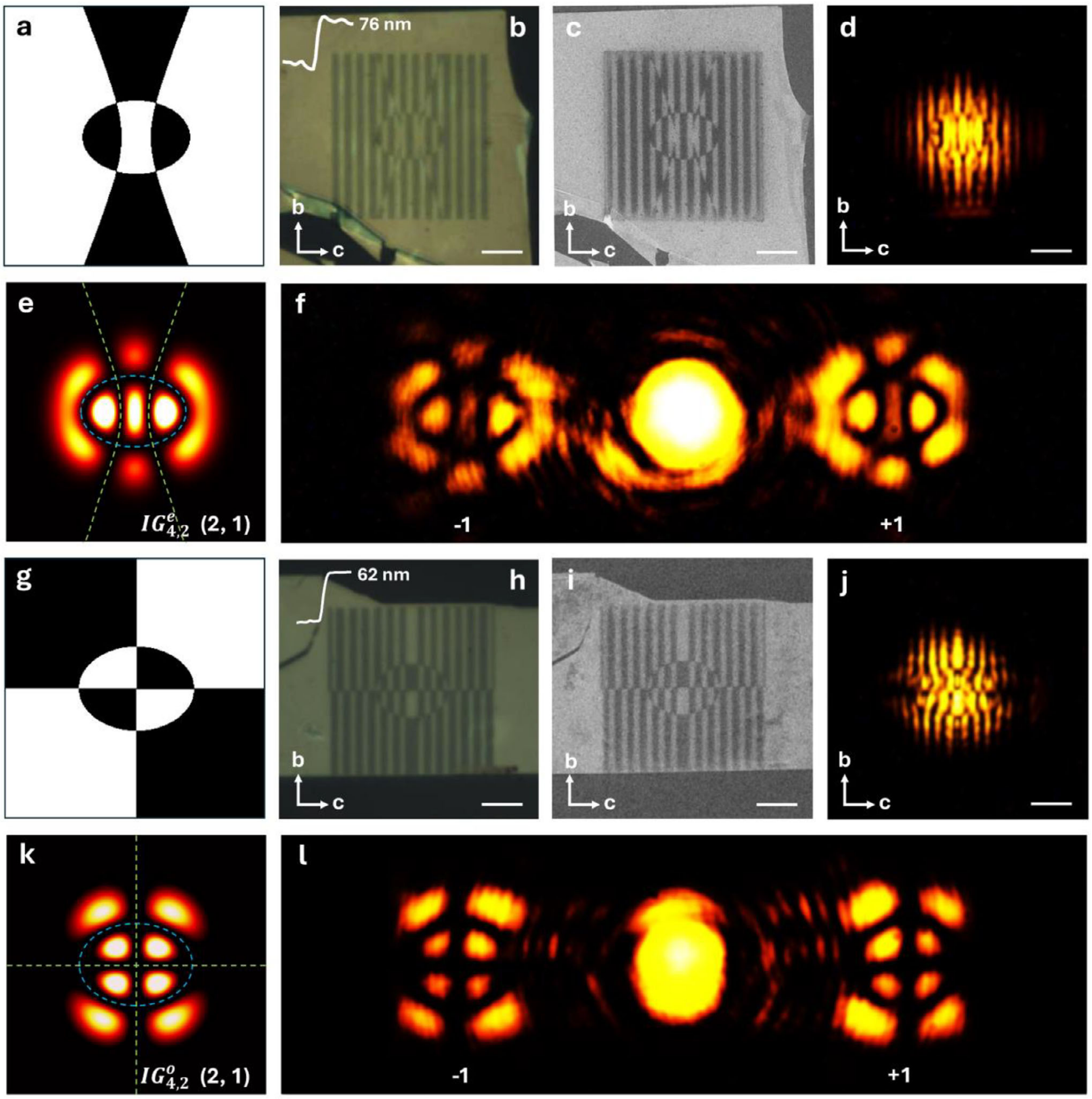

FIGURE 2 | Generation of the second-harmonic $IG^e_{4,\,2}$ and $IG^o_{4,\,2}$ beams using $NbOBr_2$ holograms. (a) Calculated phase profile of the $IG^e_{4,\,2}$ beam, with black and white regions indicating phases of 0 and π, respectively. (b) Optical microscope image, (c) SEM image, and (d) SHG image of the fabricated hologram for generating the $IG^e_{4,\,2}$ beam. The grating lines are aligned with the crystallographic *b*-axis. The AFM line scan is shown in the inset of the optical image. (e) Calculated intensity profile of the $IG^e_{4,\,2}$ beam with the hyperbolic and elliptic nodal lines shown as green and blue dashed lines, respectively. The values in the brackets $(m, (p-m)/2)$ represent the numbers of hyperbolic and elliptic nodal lines, respectively. (f) Fourier-plane SHG image of the hologram showing the generated $IG^e_{4,\,2}$ beam in the ±1 diffraction order. (g–l) Corresponding images for the generation of the $IG^o_{4,\,2}$ beam. All scale bars are 10 μm.

where Λ is the grating period, which is chosen to be 3 μm. The corresponding diffraction angle θ_{SHG} of the second-harmonic IG beam is determined to be around 15.1° according to the grating equation of $\theta_{SHG} = sin^{-1}(\lambda_{SHG}/\Lambda)$ with the SHG wavelength λ_{SHG} of 780 nm.

The calculated phase profile of the $IG^e_{4,\,2}$ beam at the $z = 0$ plane is plotted in Figure 2a, depicting multiple phase discontinuities between 0 and π, which correspond to the nodal lines of beam structure and are associated with the intensity minima of the beam. Figure 2b,c shows the optical microscope image and the scanning electron microscopy (SEM) image of the fabricated binary grating hologram patterned using focused ion beam (FIB) on an area 40×40 μm^2. The grating lines are aligned with the crystallographic *b*-axis of the $NbOBr_2$ flake corresponding to the orientation of the maximum SHG intensity. From the line scan of the AFM image of the flake shown in the inset of Figure 2b, the thickness of the flake is estimated as 76 nm. The corresponding SHG image of the hologram in the real plane is shown in Figure 2d under the excitation of 1560 nm pump laser with the excitation polarization angle set along the *b*-axis. The spot diameter of the pump beam at the hologram plane is around 38 µm, which illuminates most of the hologram area. Figure 2e displays the calculated intensity distribution of the $IG^e_{4,2}$ beam using Equation (2). Figure 2f shows the SHG image from the hologram in the Fourier plane, which demonstrates the generation of the $IG^e_{4,2}$ beam in the ±1 diffraction order. It is observed that the generated $IG^e_{4,2}$ beam is in good agreement with the theoretical beam profile, where the beam structure consists of two hyperbolic nodal lines and one elliptic nodal line corresponding to the phase discontinuities shown in Figure 2a. It is noted that for the IG beam with order p and degree m, the number of hyperbolic nodal lines and the number of elliptic nodal lines are equal to the values of m and $(p-m)/2$, respectively. Figure 2g shows the calculated phase profile of the $IG^o_{4,2}$ mode at the $z = 0$ plane. The optical microscope image and the SEM image of the fabricated hologram are shown in Figure 2h,i, with the grating lines aligned with the *b*-axis. The line scan of the AFM image is also plotted in the inset of Figure 2h giving the estimated flake thickness of 62 nm. The real-plane SHG image of the hologram is shown in Figure 2j. The calculated intensity profile of the $IG^o_{4,2}$ beam obtained from Equation (3) is plotted in Figure 2k. The Fourier-plane SHG image of the hologram is displayed in Figure 2l, demonstrating the generation of the $IG^o_{4,2}$ beam in the first diffraction order, which shows good agreement with the calculated beam profile. It is shown that the beam structure contains two hyperbolic nodal lines oriented along the horizontal and vertical directions, as well as one elliptic nodal line.

To demonstrate the versatility of the designed holograms in producing the second-harmonic IG beams, we further study the generation of the higher-order $IG^e_{5,3}$ and $IG^o_{5,3}$ beams. The calculated phase profile of the $IG^e_{5,3}$ is plotted in Figure 3a, showing three hyperbolic nodal lines and one elliptic nodal line where the phase discontinuities occur. The optical microscope image and the SEM image of the hologram patterned on an $NbOBr_2$ flake are shown in Figure 3b,c, with the grating lines orientated along the crystallographic *b*-axis. The thickness of the flake is estimated as 78 nm, as shown by the AFM line plot in the inset of Figure 3b. The SHG images of the hologram in the real plane and the Fourier plane are presented in Figure 3d,f, respectively, showing the $IG^e_{5,3}$ beam generation in the first diffraction order. The beam profile of the generated $IG^e_{5,3}$ beam matches well with the calculated intensity profile of the beam as plotted in Figure 3e, where three hyperbolic nodal lines and one elliptic nodal line are observed in the beam structure. The $IG^e_{5,3}$ beam is observed to be wider than the $IG^e_{4,2}$ beam by comparing the SHG images of the two beams in Figures 2f and 3f, which is consistent with the theoretical prediction that the IG modes with higher mode indices possess larger beam widths [1]. Next, the binary grating hologram for generating the $IG^o_{5,3}$ mode is designed and characterized. Figure 3g plots the calculated phase profile. The optical microscope image and the SEM image of the fabricated hologram on the $NbOBr_2$ flake with the thickness of 66 nm are displayed in Figure 3h,i. As in the case of the other holograms, the grating lines are designed to be aligned with the *b*-axis of the crystal. The real-plane and the Fourier-plane SHG images of the hologram are shown in Figure 3j,l, respectively, while the calculated intensity profile of the $IG^o_{5,3}$ beam is displayed in Figure 3k. It is demonstrated that the second-harmonic $IG^o_{5,3}$ beam is generated in the first diffraction order, showing good agreement with the theoretical intensity profile.

To quantify the fidelity of the generated IG beams, the experimental beam profiles are compared with the simulated ones using the mean squared error (MSE) and the structural similarity index measure (SSIM) as quantitative metrics of theory-experiment agreement. The MSE is used for comparing the average squared difference between the corresponding pixel intensity values of the experimental and simulated beam profiles. To further characterize the changes in beam structure details between the captured and simulated beam images, the SSIM is employed as a perceptual metric for image quality assessment in quantifying the perceived similarity between the experimental and simulated beam profiles [41]. For perfect agreement between the experimental and simulated beam profiles, the MSE equals zero, and the SSIM equals one. For the four different IG beams generated at the ±1 diffraction order, the MSE value is in the range of 0.013–0.029, and the SSIM value is in 0.389–0.815. The generated $IG^o_{4,2}$ beams in Figure 2l have the lowest MSE values of 0.013 and 0.018 for the −1 and +1 diffraction order, showing low noise and high fidelity for the generated beam profiles, while the highest SSIM values of 0.815 and 0.762 are also achieved for the −1 and +1 diffraction order, giving high perceptual image quality for the generated beams. The $IG^e_{4,2}$ beams in Figure 2f exhibit the highest MSE values with 0.029 and 0.027 for the −1 and +1 diffraction orders, presenting relatively high noise due to the interference effect from the central beam spot corresponding to the zeroth diffraction order. Furthermore, the $IG^e_{5,3}$ beams in Figure 3f have the lowest SSIM values with 0.389 and 0.515 for the −1 and +1 diffraction orders, showing relatively low perceptual image quality due to the weak optical intensity in the beam center area.

Furthermore, the anisotropic SHG responses of the fabricated holograms are studied. A half-wave plate is used to rotate the linear polarization of the pump beam. The polarization-dependent SHG intensities for the $IG^e_{4,2}$, $IG^o_{4,2}$, $IG^e_{5,3}$ and $IG^o_{5,3}$ beams are plotted as red dots in Figure 4a–d, exhibiting highly anisotropic SHG responses with two-lobe profiles where the intensity maxima occur along the crystallographic *b*-axis of the crystal. For comparison, the polarization-dependent SHG intensities for the corresponding bare flakes are also plotted in Figure 4 as black dots, which match well with the measurements from the holograms. The measured anisotropy ratio, defined as the ratio between the maximum SHG intensity and the minimum SHG intensity is calculated to be in the range of 7.36–7.77 for the bare flakes and 6.54–6.99 for the IG beams, as listed in Table 1. The variations in the anisotropy ratio between the bare flakes can be attributed to the multiple exfoliation process of the $NbOBr_2$ crystal [37, 42], while the variations between the bare flakes and the fabricated holograms are attributed to the contamination of the crystal by gallium ions during the FIB milling process [36]. The theoretical fits using Equation (1) for the polarization-dependent SHG intensities are also plotted in Figure 4 as solid lines for the bare flakes and the holograms, showing good agreement with the measurements. Based on the theoretical fits, the relative magnitudes of the second-order nonlinear susceptibility elements of $NbOBr_2$ crystal are retrieved

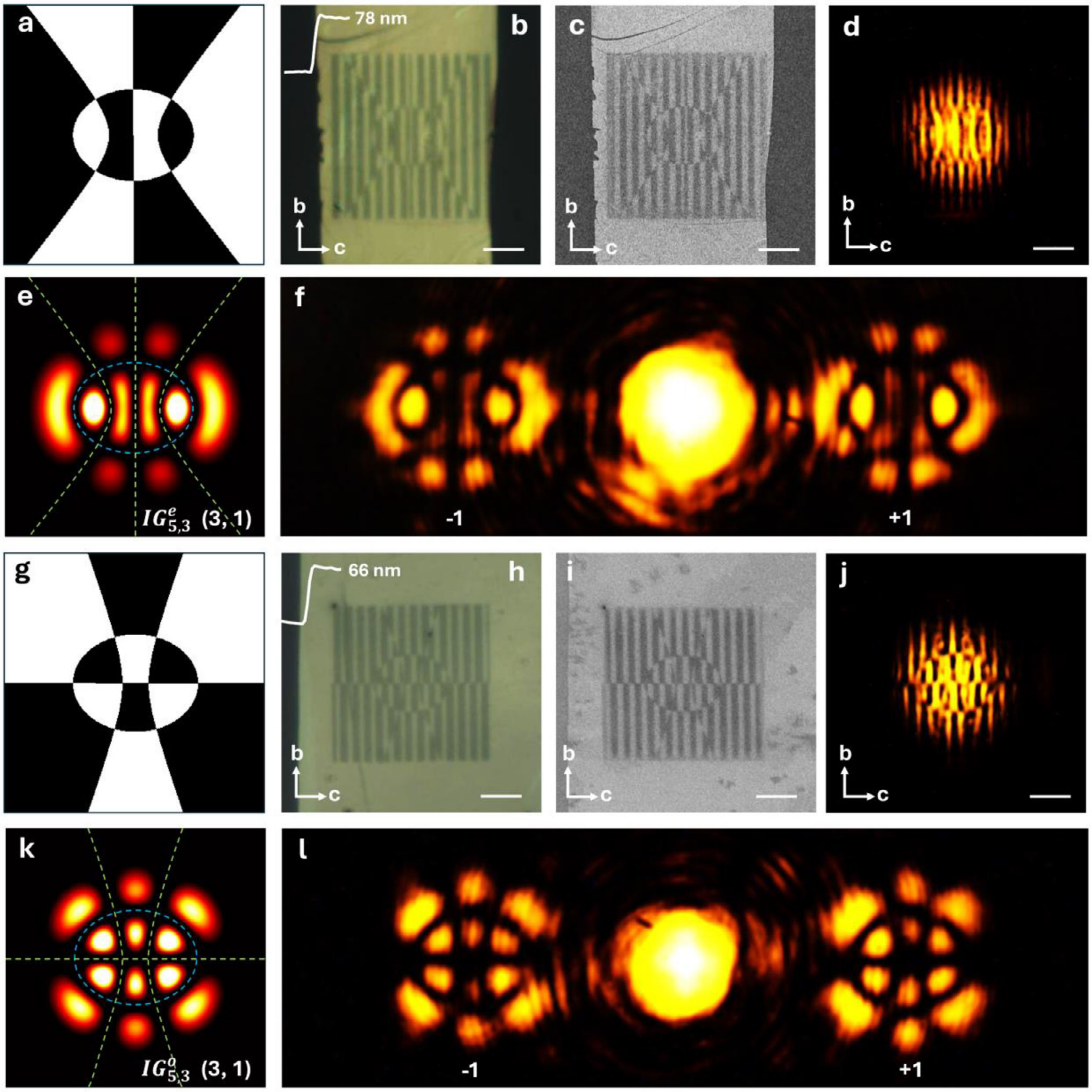

FIGURE 3 | Generation of the second-harmonic $IG^e_{5,\,3}$ and $IG^o_{5,\,3}$ beams using $NbOBr_2$ holograms. (a) Calculated phase profile of the $IG^e_{5,\,3}$ beam, with black and white regions indicating phases of 0 and π, respectively. (b) Optical microscope image, (c) SEM image, and (d) SHG image of the fabricated hologram to generate the $IG^e_{5,\,3}$ beam. The grating lines are aligned with the crystallographic *b*-axis. The AFM line scan is shown in the inset of the optical image. (e) Calculated intensity profile of the $IG^e_{5,\,3}$ beam with the hyperbolic and elliptic nodal lines shown as green and blue dashed lines, respectively. The values in the brackets (m, $(p{-}m)/2$) represent the numbers of hyperbolic and elliptic nodal lines, respectively. (f) Fourier-plane SHG image of the hologram showing the generated $IG^e_{5,\,3}$ beam in the ±1 diffraction order. (g–l) Corresponding images for the generation of the $IG^o_{5,\,3}$ beam. All scale bars are 10 µm.

for the bare flakes and the IG beams, which are listed in Table 1. The relative magnitude of the element $\chi^{(2)}_{bcc}$ is in the range of 0.36-0.39 for different samples with the average value of 0.38 ± 0.01, compared to the element $\chi^{(2)}_{bbb}$ which is normalized to unity. The theoretical anisotropy ratio can be expressed as $|\chi^{(2)}_{bbb}/\chi^{(2)}_{bcc}|^2$, and its value changes in the range of 7.30–7.72 for the bare flakes and 6.57–7.30 for the IG beams, which is consistent with the measured anisotropy ratio.

The SHG conversion efficiencies of the generated IG beams are also calculated. The SHG conversion efficiency η_{SHG} of the hologram is defined as the ratio of the total SHG power to the excitation pump power. The excitation linear polarization is along the crystallographic *b*-axis, corresponding to the maximum SHG intensity. The excitation pump power is 75 mW, which corresponds to a peak irradiance of 0.92 GW/cm^2 at the hologram plane. The SHG conversion efficiencies of the holograms are

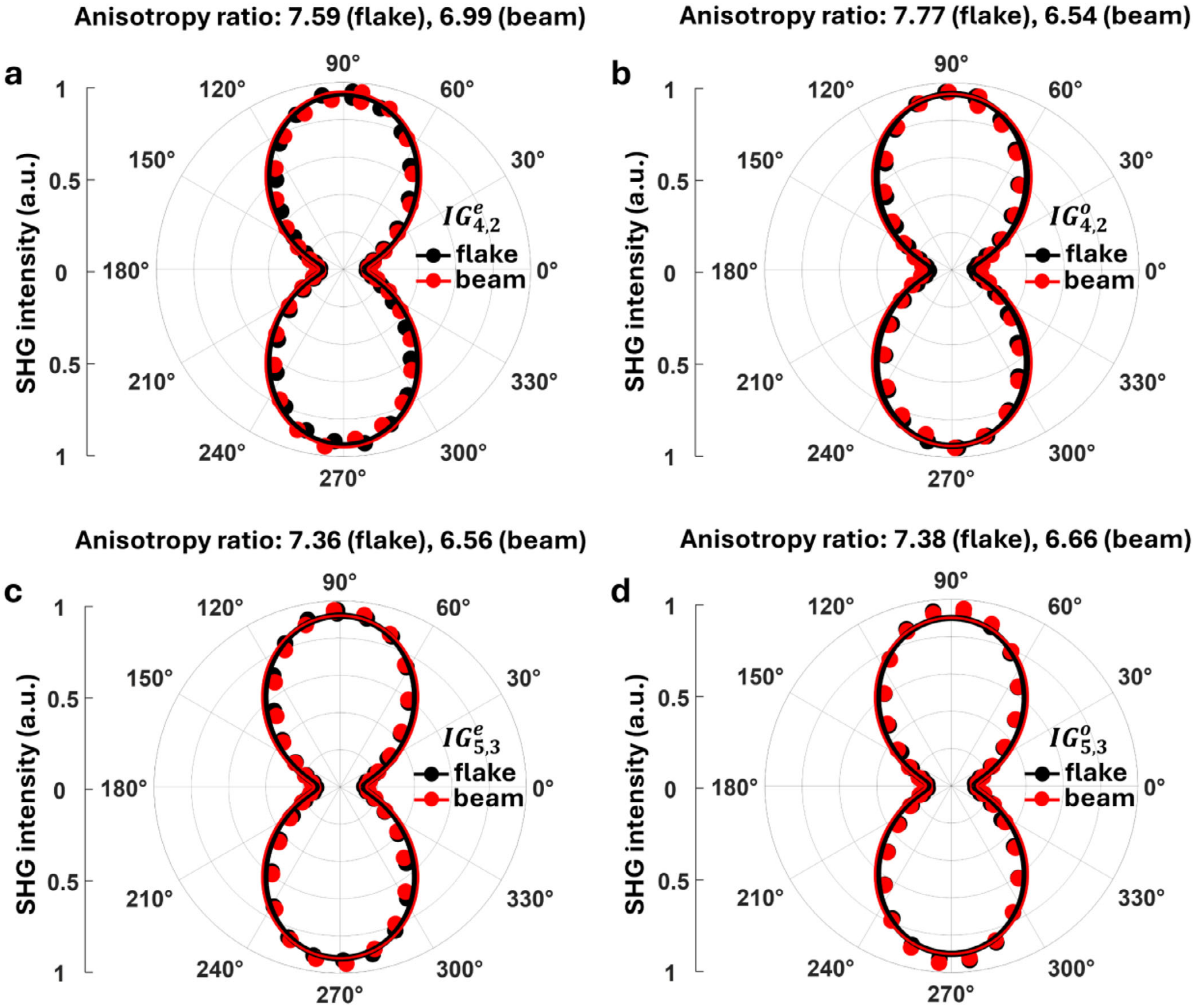

FIGURE 4 | Measured polarization-dependent SHG intensities of the bare flakes (black dots) and the generated IG beams (red dots) for (a) $IG^{e}_{4,\ 2}$, (b) $IG^{o}_{4,\ 2}$, (c) $IG^{e}_{5,\ 3}$, and (d) $IG^{o}_{5,\ 3}$ beams. The corresponding theoretical fits for the bare flakes and the IG beams are plotted as black and red solid lines, respectively.

calculated as 4.56×10^{-10}, 4.35×10^{-10}, 5.26×10^{-10}, and 4.14×10^{-10} for the $IG^{e}_{4,\ 2}$, $IG^{o}_{4,2}$, $IG^{e}_{5,\ 3}$, and $IG^{o}_{5,3}$ holograms, respectively. The SHG conversion efficiency of the IG beam is defined as $\eta_{CE} = \eta_{SHG} \cdot \eta_{DE}$, where η_{DE} is the diffraction efficiency defined as the fraction of the total SHG power directed into the first diffraction order. The diffraction efficiencies are calculated as 40.66%, 46.81%, 35.95% and 43.06% for the $IG^{e}_{4,\ 2}$, $IG^{o}_{4,2}$, $IG^{e}_{5,\ 3}$ and $IG^{o}_{5,3}$ holograms, respectively. Finally, the SHG conversion efficiencies of the generated IG beams are determined to be 1.85×10^{-10}, 2.04×10^{-10}, 1.89×10^{-10}, and 1.78×10^{-10} for the $IG^{e}_{4,\ 2}$, $IG^{o}_{4,2}$, $IG^{e}_{5,\ 3}$ and $IG^{o}_{5,3}$ beams, respectively.

3 | Conclusion

The generation of highly anisotropic second-harmonic IG beams has been demonstrated with the binary grating holograms patterned on ultrathin $NbOBr_2$ flakes. The phase profiles of the IG beams are encoded into the grating holograms in the form of binary modulation of the second-order nonlinear susceptibility of $NbOBr_2$ crystal for generating the second-harmonic IG beams in the first diffraction order. The IG beams are produced for both even and odd modes with different mode indices. The polarization-dependent measurements reveal highly anisotropic SHG responses of the generated IG beams which are attributed to the unique crystal structure of $NbOBr_2$. From the theoretical fits of the measured polarization-dependent SHG intensities, the relative magnitudes of the second-order nonlinear susceptibility elements of $NbOBr_2$ crystal are extracted. These results provide new directions in building chip-scale ultrathin polarization-sensitive photonic devices to generate complex optical beams for applications in optical trapping, optical communication and quantum optics. It is noted that $NbOBr_2$ crystal exhibits strong non-volatile SHG modulation under an external electric field due to its pronounced in-plane ferroelectricity, which makes it suitable for realizing electrically reconfigurable nonlinear optical

TABLE 1 | Extracted relative magnitudes of the second-order nonlinear susceptibility elements of $NbOBr_2$ crystal along with the theoretical and measured anisotropy ratios for the bare flakes and the IG beams.

Sample	$\chi^{(2)}_{bbb}$	$\chi^{(2)}_{bcc}$	$\lvert\chi^{(2)}_{bbb}/\chi^{(2)}_{bcc}\rvert^2$	Measured anisotropy ratio
$IG^e_{4,2}$ flake/beam	1	0.36/0.37	7.72/7.30	7.59/6.99
$IG^o_{4,2}$ flake/beam	1	0.36/0.39	7.72/6.57	7.77/6.54
$IG^e_{5,3}$ flake/beam	1	0.37/0.39	7.30/6.57	7.36/6.56
$IG^o_{5,3}$ flake/beam	1	0.37/0.39	7.30/6.57	7.38/6.66

devices in future photonic integrated circuits [43]. Moreover, it is known that the Curie temperature for ferroelectric to paraelectric phase transition of $NbOBr_2$ crystal is 283 K [44], which can be further utilized for building temperature-tunable nonlinear photonic platforms.

4 | Experimental Section

4.1 | Sample Preparation

The $NbOBr_2$ flakes are exfoliated from the bulk crystal (Nanjing MKNANO Tech. Co., Ltd.) using polydimethylsiloxane films and transferred to glass substrates using the dry transfer technique. The glass substrates are cleaned using acetone and isopropyl alcohol before the flake transfer. The samples are coated with a water-soluble conductive polymer layer for better surface charge dissipation during the subsequent FIB process. The holograms are patterned using FIB (FEI Helios Nanolab 600) on an area of 40 × 40 μm^2. After patterning, the conductive polymer is removed by rinsing the samples with deionized water, followed by blow-drying with nitrogen gas.

4.2 | Optical Setup

The pump laser beam at 1560 nm wavelength (Calmer fiber laser, pulse width 90 fs, repetition rate 80 MHz) is focused on the sample using a 4× objective lens with NA = 0.12. A combination of a linear polarizer and a half-wave plate is utilized to rotate the excitation linear polarization. The transmitted signal through the sample is collected using a 20× objective lens with NA = 0.42 and then passed through a 900 nm shortpass filter and a 780 nm bandpass filter to select the generated SHG signal. The SHG images of the holograms are recorded either in the real plane or the Fourier plane using a color charge-coupled device camera. The SHG spectrum is measured with an optical spectrometer (Horiba, iHR550).

Acknowledgements

The authors acknowledge the support from the National Science Foundation under Grant Nos. DMR-2412218, DMR-2412219, ECCS-2226875, and ECCS-2226948. The authors thank the facility support from the Materials Research Center at Missouri S&T.

Conflicts of Interest

The authors declare no conflicts of interest.

Data Availability Statement

The data that support the findings of this study are available from the corresponding author upon reasonable request.

References

1. M. A. Bandres and J. C. Gutiérrez-Vega, "Ince–Gaussian Beams," *Optics Letters* 29 (2004): 144–146, https://doi.org/10.1364/OL.29.000144.

2. M. A. Bandres and J. C. Gutiérrez-Vega, "Ince–Gaussian Modes Of The Paraxial Wave Equation And Stable Resonators," *Journal of the Optical Society of America A* 21 (2004): 873–880, https://doi.org/10.1364/JOSAA.21.000873.

3. M. Woerdemann, C. Alpmann, and C. Denz, "Optical Assembly Of Microparticles Into Highly Ordered Structures Using Ince–Gaussian Beams," *Applied Physics Letters* 98 (2011): 111101, https://doi.org/10.1063/1.3561770.

4. S. Sakpal, G. Milione, M.-J. Li, et al., "Stability of Ince–Gaussian Beams in Elliptical Core Few-Mode Fibers," *Optics Letters* 43 (2018): 2656–2659, https://doi.org/10.1364/OL.43.002656.

5. H. T. Eyyuboğlu, "Propagation Analysis of Ince-Gaussian Beams in Turbulent Atmosphere," *Applied Optics* 53 (2014): 2290.

6. D. G. Pires, J. C. A. Rocha, A. J. Jesus-Silva, and E. J. S. Fonseca, "Optical Mode Conversion Through Nonlinear Two-wave Mixing," *Physical Review A* 100 (2019): 043819, https://doi.org/10.1103/PhysRevA.100.043819.

7. D. G. Pires, J. C. A. Rocha, M. V. E. C. da Silva, A. J. Jesus-Silva, and E. J. S. Fonseca, "Mixing Ince–Gaussian Modes Through Sum-Frequency Generation," *Journal of the Optical Society of America B* 37 (2020): 2815–2821, https://doi.org/10.1364/JOSAB.401001.

8. H.-R. Yang, H.-J. Wu, W. Gao, C. Rosales-Guzmán, and Z.-H. Zhu, "Parametric Upconversion of Ince–Gaussian Modes," *Optics Letters* 45 (2020): 3034–3037, https://doi.org/10.1364/OL.393146.

9. M. Krenn, R. Fickler, M. Huber, et al., "Entangled Singularity Patterns of Photons in Ince-Gauss Modes," *Physical Review A* 87 (2013): 012326, https://doi.org/10.1103/PhysRevA.87.012326.

10. B. Baghdasaryan and S. Fritzsche, "Enhanced Entanglement From Ince-Gaussian Pump Beams in Spontaneous Parametric Down-conversion," *Physical Review A* 102 (2020): 052412, https://doi.org/10.1103/PhysRevA.102.052412.

11. Y. Li, X. B. Hu, B. Perez-Garcia, et al., "Classically Entangled Ince–Gaussian Modes," *Applied Physics Letters* 116 (2020): 221105, https://doi.org/10.1063/5.0011142.

12. E. G. Abramochkin, V. V. Kotlyar, and A. A. Kovalev, "Structurally Invariant Higher-Order Ince-Gaussian Beams and Their Expansions Into Hermite-Gaussian or Laguerre-Gaussian Beams," *Applied Sciences* 14 (2024): 1759, https://doi.org/10.3390/app14051759.

13. M. Woerdemann, C. Alpmann, M. Esseling, and C. Denz, "Advanced Optical Trapping by Complex Beam Shaping," *Laser & Photonics Reviews* 7 (2013): 839–854, https://doi.org/10.1002/lpor.201200058.

14. W. T. Buono and A. Forbes, "Nonlinear Optics With Structured Light," *Opto-Electronic Advances* 5 (2022): 210174, https://doi.org/10.29026/oea.2022.210174.

15. A. Forbes, F. Nothlawala, and A. Vallés, "Progress in Quantum Structured Light," *Nature Photonics* 19 (2025): 1291–1300, https://doi.org/10.1038/s41566-025-01795-x.

16. J. B. Bentley, J. A. Davis, M. A. Bandres, and J. C. Gutiérrez-Vega, "Generation of Helical Ince-Gaussian Beams With a Liquid-crystal Display," *Optics Letters* 31 (2006): 649–651, https://doi.org/10.1364/OL.31.000649.

17. Y.-X. Ren, Z.-X. Fang, L. Gong, K. Huang, Y. Chen, and R.-D. Lu, "Dynamic Generation of Ince-Gaussian Modes With a Digital Micromirror Device," *Journal of Applied Physics* 117 (2015): 133106, https://doi.org/10.1063/1.4915478.

18. D. Aguirre-Olivas, G. Mellado-Villaseñor, D. Sánchez-de-la-Llave, and V. Arrizón, "Efficient generation of Hermite–Gauss and Ince–Gauss beams Through kinoform phase elements," *Applied Optics* 54 (2015): 8444–8452, https://doi.org/10.1364/AO.54.008444.

19. H. Ahmed, M. A. Ansari, L. Paterson, J. Li, and X. Z. Chen, "Metasurface for Engineering Superimposed Ince-Gaussian Beams," *Advanced Materials* 36 (2024): 2312853, https://doi.org/10.1002/adma.202312853.

20. M.-Y. Wang, J. Tang, H.-J. Wang, et al., "Generation of Second-harmonic Ince-Gaussian Beams," *Applied Physics Letters* 113 (2018): 081105, https://doi.org/10.1063/1.5041986.

21. S. K. Singh, H. Haginaka, B. J. Jackin, K. Kinashi, N. Tsutsumi, and W. Sakai, "Generation of Ince–Gaussian Beams Using Azocarbazole Polymer CGH," *Journal of Imaging* 8 (2022): 144, https://doi.org/10.3390/jimaging8050144.

22. J.-C. Yang, W. Chen, L.-I. Ma, et al., "Nonlinear Photon Sieves for High-Fidelity Wavefront Engineering," *Laser & Photonics Reviews* 19 (2025): 01117, https://doi.org/10.1002/lpor.202501117.

23. J. W. You, S. R. Bongu, Q. Bao, and N. C. Panoiu, "Nonlinear Optical Properties and Applications of 2D Materials: Theoretical and Experimental Aspects," *Nanophotonics* 8 (2019): 63–97, https://doi.org/10.1515/nanoph-2018-0106.

24. J. Zhang, W. Zhao, P. Yu, G. Yang, and Z. Liu, "Second Harmonic Generation in 2D Layered Materials," *2D Materials* 7 (2020): 042002, https://doi.org/10.1088/2053-1583/abaf68.

25. W. Huang, Y. Xiao, F. Xia, X. Chen, and T. Zhai, "Second Harmonic Generation Control in 2D Layered Materials: Status and Outlook," *Advanced Functional Materials* 34 (2024): 2310726, https://doi.org/10.1002/adfm.202310726.

26. H. Liu, Z. Li, Y. Yu, et al., "Nonlinear optical properties of anisotropic two-dimensional layered materials for ultrafast photonics," *Nanophotonics* 9 (2020): 1651–1673, https://doi.org/10.1515/nanoph-2019-0573.

27. S. H. Suk, S. B. Seo, Y. S. Cho, J. Wang, and S. Sim, "Ultrafast Optical Properties and Applications of Anisotropic 2D Materials," *Nanophotonics* 13 (2024): 107–154, https://doi.org/10.1515/nanoph-2023-0639.

28. A. Dasgupta, J. Gao, and X. Yang, "Anisotropic Third-Harmonic Generation in Layered Germanium Selenide," *Laser & Photonics Reviews* 14 (2020): 1900416, https://doi.org/10.1002/lpor.201900416.

29. I. Abdelwahab, B. Tilmann, Y. Wu, et al., "Giant Second-harmonic Generation in Ferroelectric $NbOI_2$," *Nature Photonics* 16 (2022): 644–650, https://doi.org/10.1038/s41566-022-01021-y.

30. Q. Guo, X. Qi, L. Zhang, et al., "Ultrathin Quantum Light Source With van der Waals $NbOCl_2$ Crystal," *Nature* 613 (2023): 53–59, https://doi.org/10.1038/s41586-022-05393-7.

31. L. Ye, W. Zhou, D. Huang, et al., "Manipulation of Nonlinear Optical Responses in Layered Ferroelectric Niobium Oxide Dihalides," *Nature Communications* 14 (2023): 5911, https://doi.org/10.1038/s41467-023-41383-7.

32. W. Chen, S. Zhu, R. Duan, et al., "Extraordinary Enhancement of Nonlinear Optical Interaction in $NbOBr_2$ Microcavities," *Advanced Materials* 36 (2024): 2400858, https://doi.org/10.1002/adma.202400858.

33. H. Wang, Q. Chen, Y. Cao, et al., "Anisotropic Strain-Tailoring Nonlinear Optical Response in van der Waals $NbOI_2$," *Nano Letters* 24 (2024): 3413–3420, https://doi.org/10.1021/acs.nanolett.4c00039.

34. T. Fu, K. Bu, X. Sun, et al., "Manipulating Peierls Distortion in van der Waals $NbOX_2$ Maximizes Second-Harmonic Generation," *Journal of the American Chemical Society* 145 (2023): 16828–16834, https://doi.org/10.1021/jacs.3c04971.

35. M. Wu, M. An, Z. Lou, et al., "Manipulating Anisotropy of Second Harmonic Generation in $NbOI_2$ via Precise Strain Engineering," *Advanced Functional Materials* 36 (2026): 16389.

36. J. Deka, X. Yang, and J. Gao, "Anisotropic and Temperature-Tunable Second-Harmonic Vortex Generation in Ferroelectric NbOCl2 Holograms," *Laser & Photonics Reviews* 20 (2026): 01523.

37. J. Deka, J. Gao, and X. Yang, "Anisotropic Second- and Third-Harmonic Hermite–Gaussian Beam Generation With $NbOI_2$ Holograms," *Advanced Photonics Research* 6 (2025): 2500188, https://doi.org/10.1002/adpr.202500188.

38. J. Zhao, Y. Zhao, Y. Guo, et al., "Layered Metal-Halide Perovskite Single-Crystalline Microwire Arrays for Anisotropic Nonlinear Optics," *Advanced Functional Materials* 31 (2021): 2105855, https://doi.org/10.1002/adfm.202105855.

39. D. Li, C. Wei, J. Song, et al., "Anisotropic Enhancement of Second-Harmonic Generation in Monolayer and Bilayer MoS_2 by Integrating With TiO_2 Nanowires," *Nano Letters* 19 (2019): 4195–4204, https://doi.org/10.1021/acs.nanolett.9b01933.

40. J. Beck and C. Kusterer, "Crystal Structure of $NbOBr_2$," *Zeitschrift für anorganische und allgemeine Chemie* 632 (2006): 2193–2194, https://doi.org/10.1002/zaac.200600171.

41. Z. Wang, A. C. Bovik, H. R. Sheikh, and E. P. Simoncelli, "Image Quality Assessment: From Error Visibility to Structural Similarity," *IEEE Transactions on Image Processing* 13 (2004): 600–612, https://doi.org/10.1109/TIP.2003.819861.

42. H. Sar, J. Gao, and X. Yang, "In-plane Anisotropic Third-harmonic Generation From Germanium Arsenide Thin Flakes," *Scientific Reports* 10 (2020): 14282, https://doi.org/10.1038/s41598-020-71244-y.

43. S. H. Chae, X. Gong, R. Duan, et al., "Electrically Tunable Ferroelectric $NbOBr_2$-Integrated Nonlinear Photonics," *Preprint* (2025), https://doi.org/10.21203/rs.3.rs-6420732/v1.

44. Y. Jia, M. Zhao, G. Gou, X. C. Zeng, and J. Li, "Niobium Oxide Dihalides NbOX2: A New family of Two-dimensional van der Waals Layered Materials With Intrinsic Ferroelectricity and Antiferroelectricity," *Nanoscale Horizons* 4 (2019): 1113–1123, https://doi.org/10.1039/C9NH00208A.